symmetry

MDPI

Article

Co-Dominant Piezoelectric and Flexoelectric Effects in Twisted Double Bilayer Graphene

Yuanhao Wei [1,†], Yuhao Li [2,3,*,†], Hanhao Zhang [2], Shengsheng Lin [2], Takashi Taniguchi [4], Kenji Watanabe [5], Cun-Fa Gao [1] and Yan Shi [1,*]

[1] State Key Laboratory of Mechanics and Control for Aerospace Structures, Nanjing University of Aeronautics and Astronautics, Nanjing 210016, China
[2] National Laboratory of Solid-State Microstructures, School of Electronic Science and Engineering and Collaborative Innovation Center of Advanced Microstructures, Nanjing University, Nanjing 210093, China
[3] National Key Laboratory of Spintronics, Nanjing University, Suzhou 215163, China
[4] Research Center for Materials Nanoarchitectonics, National Institute for Materials Science, 1-1 Namiki, Tsukuba 305-0044, Japan
[5] Research Center for Electronic and Optical Materials, National Institute for Materials Science, 1-1 Namiki, Tsukuba 305-0044, Japan
* Correspondence: yuhao@nju.edu.cn (Y.L.); yshi@nuaa.edu.cn (Y.S.)
† These authors contributed equally to this work.

Abstract: Controlling the balance between piezoelectric and flexoelectric effects is crucial for tailoring the electromechanical responses of a material. In twisted graphene, it is found that the electromechanical response near the domain walls (DWs) is dominated by either the flexoelectric effect as in twisted bilayer graphene (tBLG) or the piezoelectric effect as in twisted monolayer–bilayer graphene (tMBG). The codominance of both effects in a single system is rare. Here, utilizing lateral piezoresponse force microscopy (LPFM), we show that piezoelectric and flexoelectric effects can coexist and are equally important in twisted double bilayer graphene (tDBG), termed as the piezo-flexoelectric effect. Unlike tBLG and tMBG, distinctive two-step LPFM spatial profiles are captured across the moiré DWs of tDBG. By decomposing the LPFM signal into axisymmetric and antisymmetric components, we find that the angular dependence of both components satisfies sinusoidal relations. Quantitatively, the in-plane piezoelectric coefficient of DWs in tDBG is determined to be 0.15 pm/V by dual AC resonance tracking (DART) LPFM measurement. The conclusion is further supported by continuum mechanics simulations. Our results demonstrate that the stacking configuration serves as a powerful tuning knob for modulating the electromechanical responses of twisted van der Waals materials.

Keywords: lateral piezoresponse force microscopy; twisted double bilayer graphene; flexoelectric effect; piezoelectric effect; piezo-flexoelectric effect

check for updates

Citation: Wei, Y.; Li, Y.; Zhang, H.; Lin, S.; Taniguchi, T.; Watanabe, K.; Gao, C.-F.; Shi, Y. Co-Dominant Piezoelectric and Flexoelectric Effects in Twisted Double Bilayer Graphene. *Symmetry* **2024**, *16*, 1524. https://doi.org/10.3390/sym16111524

Received: 15 October 2024
Revised: 8 November 2024
Accepted: 11 November 2024
Published: 14 November 2024

1. Introduction

The emergence of electric polarizations and enhanced electrical conductivity at DWs of non-polar materials can admit many new functional devices, such as diodes, memories and switches [1–3]. However, so far, the progress in developing these devices has been slow, partially due to the incomplete understanding of the origins of the polarization and the lack of an efficient tuning knob for the polarization. For many materials, investigations on polarization are further complicated by the presence of defect states, multiple sources and other order parameters, such as the domain boundary and piezo-flexoelectric effect [2,4]. Generally, the induced electrical polarization upon mechanical deformation can be formulated by the constitutive equation [5,6] $P_i = e_{ijk}\varepsilon_{jk} + \mu_{ijkl}\frac{\partial \varepsilon_{jk}}{\partial x_l}$, where e_{ijk} and μ_{ijkl} are the direct piezoelectric and flexoelectric coefficients; ε_{jk} and $\frac{\partial \varepsilon_{jk}}{\partial x_l}$ are the strain and strain gradient. The first term describes the piezoelectric effect, the second term corresponds to the flexoelectric effect.

Recently, twisted graphene moiré superlattices are reported to be a flexible and versatile platform for observing emergent quantum phenomena, such as superconductivity [7], correlated insulator [8], ferromagnetism [9,10] and even ferroelectricity [11,12]. In the small twist angle limit, alternating non-polar stacking domains emerge due to lattice reconstruction, and the dislocations are concentrated on the boundaries between adjacent domains, leading to clean DWs with remarkable strain and strain gradient [13]. The DW width is on the order of 10 nm, falling in the mesoscopic regime. This makes twisted graphene an ideal platform for hosting piezoelectric and flexoelectric polarizations simultaneously. In practice, previous works suggest the electromechanical responses of DWs are dominated by the flexoelectric effect [14–16] and the piezoelectric effect [16] for tBLG and tMBG, respectively, possibly due to symmetry constraints. Our previous work presented the background-signal-free LPFM signal of a tDBG sample [15]. However, the origin of electromechanical responses for tDBG are still poorly understood.

In this paper, we focus on tDBG samples, revealing distinct LPFM profiles from tBLG and tMBG. Specifically, a two-step LPFM profile was captured with identical conductive atomic force microscopy (cAFM) current changes. We propose that this two-step profile is attributed to the combination of an axisymmetric flexoelectric effect and an antisymmetric piezoelectric effect which is consistent with our continuum mechanics simulations, and we term this as the ‘piezo-flexoelectric effect’. The angular dependence of both components satisfies a sinusoidal relation, which is a typical behavior for in-plane polarization. Moreover, the in-plane piezoelectric coefficient of tDBG is determined to be 0.15 pm/V by DART LPFM.

2. Results and Discussion

Here, two Bernal-stacked graphene bilayers twist at a small in-plane angle θ relative to each other, where the least energetically favorable configuration is AB-BC stacking (red dot, labeled from top to bottom layers and hyphens for the twisted interface), forming a moiré superlattice that maximizes the energetically favorable AB-AB (blue dot) and AB-CA (green dot) at the expense of AB-BC through lattice reconstruction [17], as shown in Figure 1a. The DWs are the ‘saddle point’ (SP) stacking (black lines in Figure 1a), also known as strain soliton [18]. In our experiment, tDBG samples consist of tDBG upon a hexagonal boron nitride (h-BN) substrate. For some samples, large graphite flakes are contacted with tDBG as electrodes, and silver paste is used to connect the large graphite electrode to the external circuit for cAFM measurements. More details about sample fabrication can be found in Figure S1 and the Methods section. The principle of LPFM is illustrated in Figure 1b, which demonstrates that LPFM can only capture the component of in-plane polarization perpendicular to the cantilever axis.

Figure 1c,d show the intrinsic LPFM phase and amplitude maps of tDBG01 recovered from the background signal [15,19] (raw LPFM results are presented in Figure S2), where only DW regions show nonzero amplitude. In Figure 1e, we show the cAFM current image of the same area where the current changes at the center of the DWs. The shape of the domains is also informative. The concave–convex alternant domains can be understood as the consequence of competition between AB-AB and AB-CA stacking orders resulting in the expansion of AB-AB domains, showing a convex domain for AB-AB and a concave domain for AB-CA [15,17]. Figure 1f shows the line cuts of LPFM phase, LPFM amplitude and cAFM current along the arrows in Figure 1c–e with expected 180° phase change.

However, the amplitude and its spatial profiles are very different from previously reported tBLG and tMBG [16]. First, the maximum amplitudes of tDBG DWs are not at the center of DWs, exhibiting two-step profile amplitude, while the amplitude of a tMBG DW only gives one peak and tBLG shows two peaks. Meanwhile, the amplitude of tDBG DWs near AB-CA domains side are much higher than that near the AB-AB domain side, as marked by red and blue background in Figure 1f. This phenomenon can be understood by the enhancement and weakness of in-plane polarization on two sides of the DW. Second, the LPFM amplitude and cAFM current change at identical positions at the

DWs (dashed lines in Figure 1f). The cAFM measurement is highly sensitive to the local stacking of tDBG moiré superlattices [20–23], and an LPFM measurement can capture its in-plane polarization. Hence, the dashed lines indicate the precise SP locations between the AB-AB and AB-CA stackings, where electromechanical and electric properties change simultaneously. Specifically, for DW1, the amplitude gives a drop from 75 pm to 50 pm, while the current presents an increase from 10.3 to 15.5 nA, as marked by black arrows. The amplitudes of three tDBG DWs satisfy a sinusoidal relation (Figure 1g), which matches well with previous tMBG and tBLG results [14,16]. From the angle-dependence LPFM results of tDBG02 (see Figure S3), Figure 1h gives the in-plane polarization networks of tDBG01, which is consistent with previous tDBG results [15].

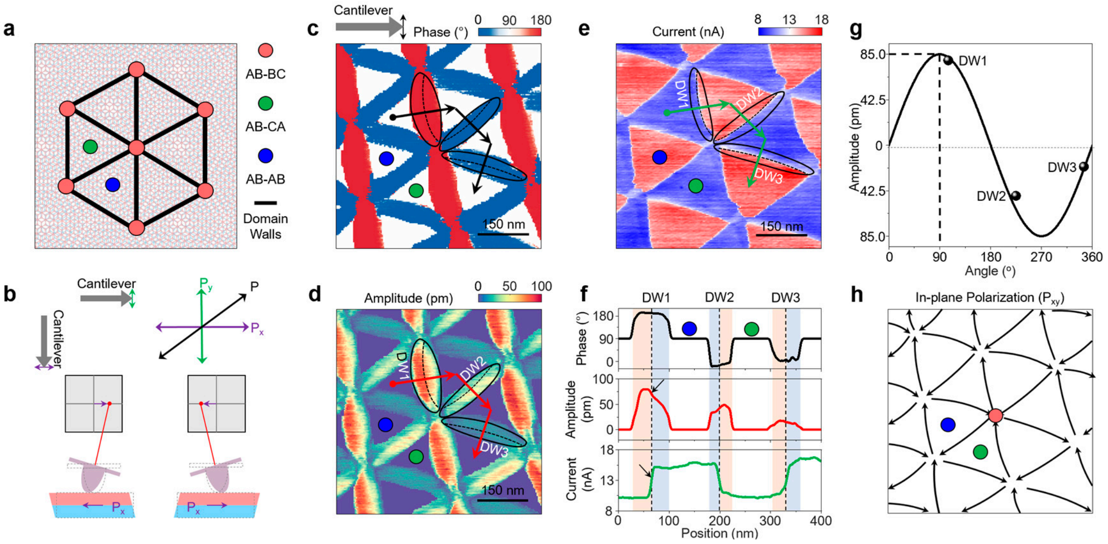

Figure 1. LPFM and cAFM mappings in tDBG sample (tDBG01). (**a**) Schematic of the tDBG moiré superlattice and relative locations of three domains, where red, green and blue dots represent AB-BC, AB-CA and AB-AB domains, respectively. (**b**) Principle of the LPFM measurement. (**c**,**d**) Phase and amplitude images of tDBG01. (**e**) Current image of the same area in (**c**,**d**). (**f**) Line cuts of the phase, amplitude and current for tDBG01 along black, red and green arrow lines and cross DW1, DW2 and DW3 in (**c**–**e**), respectively. (**g**) Sinusoidal fit of the three amplitudes vs. the cantilever axis angle relative to the DW. (**h**) Schematic of in-plane polarization networks for tDBG01 sample.

This two-step profile phenomenon can be enhanced by adjusting measurement parameters, e.g., drive frequency and cantilever-sample force. More details about the frequency-dependent LPFM amplitude of tDBG can be found in Figure S4. Figure 2a,b show the LPFM results of tDBG03 (see raw LPFM phase and amplitude images in Figure S5); its amplitude gives a clearer two-step profile than Figure 1d. Figure 2c presents line cuts of phase and amplitude along red and black arrows in Figure 2a,b. Mathematically, this two-step profile LPFM signal (red line) of DW4 can be divided into an axisymmetric vector (green line) and a centrosymmetric vector (blue line), as illustrated in Figure 2d. Hence, the axisymmetric and centrosymmetric components of line cuts in Figure 2c can be calculated, as shown in Figure 2e,f. Those decoupled LPFM results are similar to those of tMBG and tBLG in the following two aspects. First, both the axisymmetric component of tDBG and tMBG show one broad peak, and the centrosymmetric component of tDBG and tBLG give two extrema with 180° phase change. Second, the amplitudes of axisymmetric and centrosymmetric components for three DWs (DW4, DW5 and DW6) satisfy sinusoidal relations (Figure 2g), which is a typical feature for in-plane polarization [14,16]. Apart from similarity, the magnitude of the axisymmetric component of the tDBG LPFM amplitude is only twice as much as that of the centrosymmetric component, while the amplitude of tMBG is about an order of magnitude larger than that of tBLG. These similarities and differences among tBLG, tMBG and tDBG are reminiscent of the in-plane electrical polarization of tDBG generated by the combination of piezoelectric and flexoelectric effects. Noteworthily, the two-step profile is highly sensitive to scan parameters. Figure S6 shows another LPFM scan of the same area in Figure 2a,b with different drive frequencies, which gives a single-peak profile. This sensitivity to scan parameters is also shown in the tBLG sample [16].

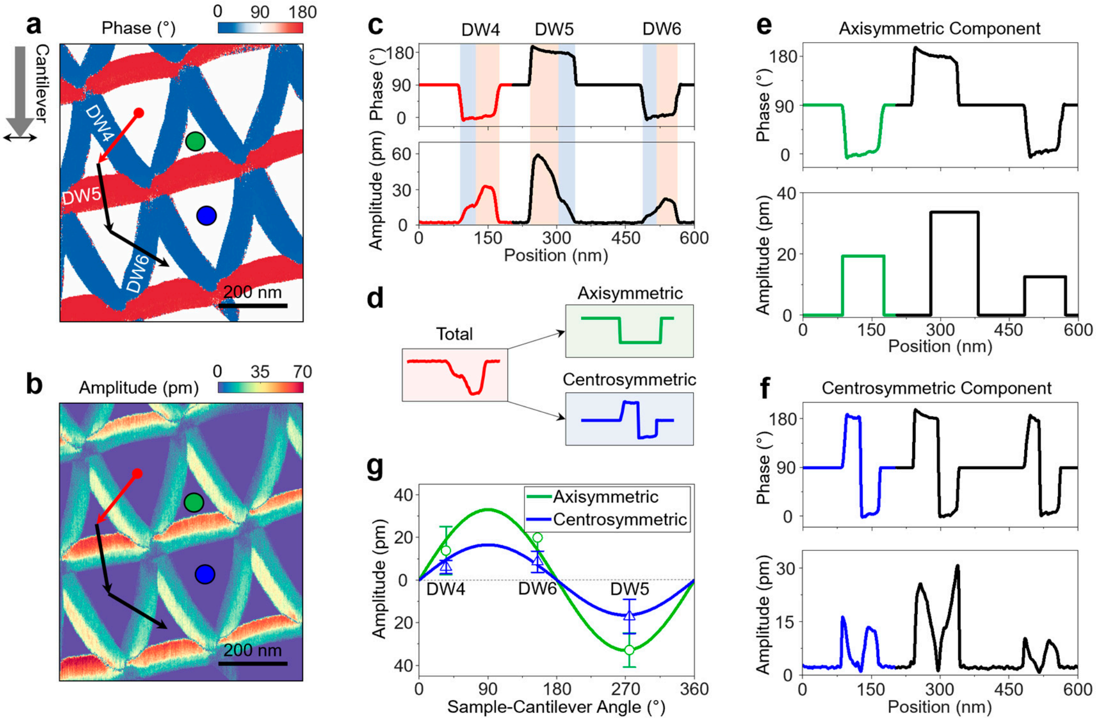

Figure 2. Decomposition of LPFM signal of tDBG sample (tDBG03). (**a**,**b**) LPFM phase and amplitude images of tDBG03. Green and blue dots represent the AB-CA and AB-AB domains, respectively. (**c**) Line cuts of the phase and amplitude for tDBG03 along the red and black arrows in (**a**,**b**). (**d**) Schematic of the decomposition process of the DW4 LPFM signal in (**c**). The red cure is the two-step LPFM signal (A·sin(θ−90°)) of DW4. The green and blue curves represent the decomposed axisymmetric and centrosymmetric components, respectively. (**e**,**f**) Line cuts of the decomposed phase and amplitude for the axisymmetric and centrosymmetric components, respectively. (**g**) Sinusoidal fits of the axisymmetric (green) and centrosymmetric (blue) amplitude, respectively.

To obtain the in-plane piezoelectric coefficients of DWs in tDBG, we performed DART LPFM measurements on tDBG04, and the typical DART LPFM amplitude and phase (decoupled from the background) maps of tDBG04 are presented in Figure 3a,b with an expected 180° phase change and three different amplitudes. One peak profile is captured in the DART LPFM measurements because the two-step profile is dependent on the scan parameters. Moreover, the centrosymmetric component of the LPFM signal has no contribution to the LPFM amplitude. Zooming in on the white dashed boxed area in Figure 3a, Figure 3c shows selected five DART LPFM amplitude maps of tDBG as the drive voltage increases from 1 V to 4.5 V (see Figure S7 for details), in which the amplitude increases significantly. Figure 3d presents the averaged amplitudes at three DWs of tDBG04 (DW7, DW8 and DW9 are marked by red, blue and green dashed polygons in Figure 3c) as a function of the drive voltage, respectively, along with their linear fits. The three fitted slopes are the three projected in-plane piezoelectric coefficients of a DW. Only when the cantilever axis is perpendicular to the DW is the fitted slope equal to the in-plane piezoelectric coefficient of the DW, except when setting sample-cantilever angle as 90°, as the in-plane piezoelectric coefficient can also be extracted by the sinusoidal fitting of the three slopes, as illustrated in Figure 3e. Consequently, the in-plane piezoelectric coefficient of a DW in tDBG is determined to be 0.15 pm/V, which is three times larger than that of tBLG and half that of tMBG [16].

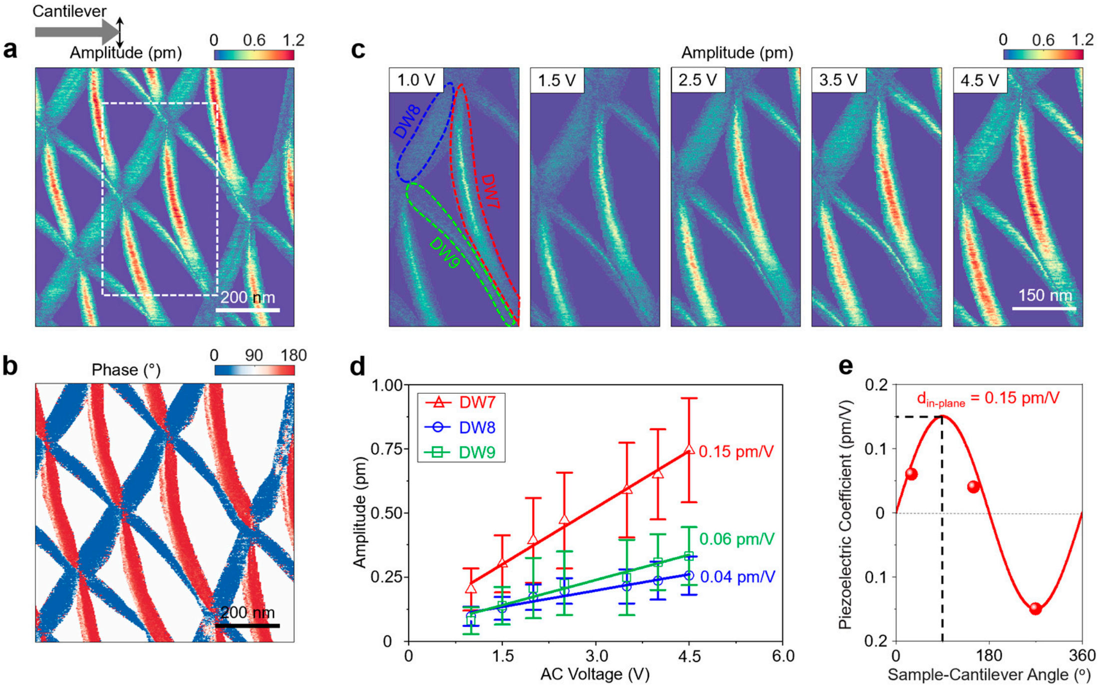

Figure 3. Determination of in-plane piezoelectric coefficient in tDBG sample (tDBG04). (**a**,**b**) Typical DART LPFM phase and amplitude images of tDBG04. (**c**) DART LPFM amplitude images of the white dashed boxed area in (**a**) under selected applied voltage from 1.0 V to 4.5 V. DW7, DW8 and DW9 are outlined by red, blue and green dashed polygons, respectively. (**d**) Averaged DART LPFM amplitude (projected deformation) at three selected DWs (DW7, DW8 and DW9) of tDBG04 as a function of the AC drive voltage, along with the linear fits. The error bars are standard deviations of the amplitude. The slopes of the linear fits, which are measured in-plane piezoelectric coefficients for three DWs in one scan, are 0.15 pm/V, 0.06 pm/V and 0.04 pm/V, respectively. (**e**) Sinusoidal fit of the three slopes versus the cantilever axis angle relative to the DW. The maximum value of the fit corresponds to the effective in-plane piezoelectric coefficient of tDBG04, which is 0.15 pm/V.

We employ continuum mechanics theory to explain the two-step LPFM profile of tDBG. When a conductive tip-induced electric field E_k is applied to the DWs of twisted graphene with an electrical polarization P_v, the induced strain ε_{ij} can be expressed as [24] $\varepsilon_{ij} = k_{im}Q_{jkmv}P_vE_k$, where k_{im} is the dielectric constant, and Q_{jkmv} is the electrostrictive coefficient. For ideal tDBG moiré superlattices, the moiré DW is shear-type along the y axis [23], as shown in Figure 4a, where u_y is the only nonzero displacement. Thus, only $\frac{\partial u_y}{\partial x}$ and $\frac{\partial^2 u_y}{\partial x^2}$ need to be taken into consideration. In Figure 4b(i), we sketch the profile of the displacement across the DW, where the profile of the displacement was adopted from Ref. [25]. For a linear constitutive relation, the in-plane piezoelectric (Figure 4b(ii)) and flexoelectric (Figure 4b(iii)) polarizations show axisymmetric and centrosymmetric profiles, respectively. Surprisingly, the linear combination of piezoelectricity and flexoelectricity gives a two-step profile (Figure 4b(iv)), which is highly consistent with the LPFM signal of tDBG; we call it 'piezo-flexoelectricity'. Based on the threefold rotational symmetry of tDBG, a two-dimensional map of the in-plane piezo-flexoelectric polarization is presented in Figure 4c. The AB-CA domains surround the in-plane polarization clockwise, and AB-AB domains enclose the in-plane polarization anticlockwise, while the magnitude of in-plane polarization near the AB-CA domain is larger than that of the AB-AB domain.

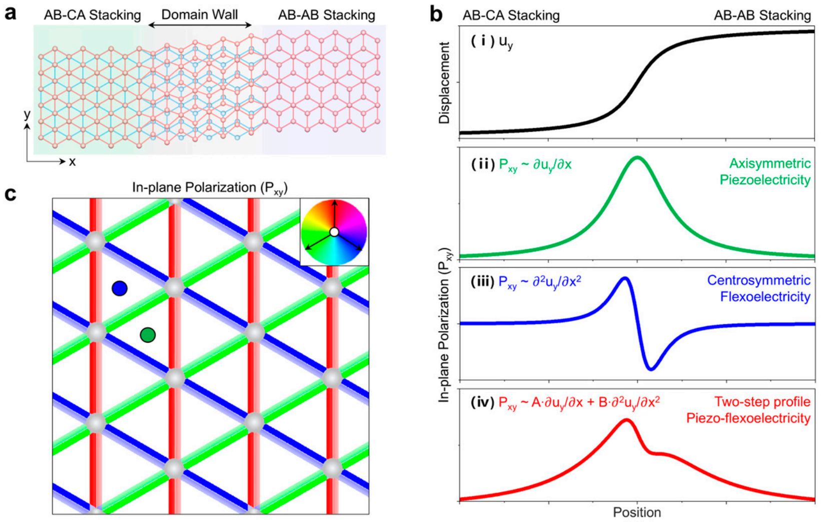

Figure 4. Continue mechanics analysis of piezoelectric and flexoelectric effects in tDBG. (**a**) Schematic of a perfect tDBG moiré DW. The red and blue hexagonal grids represent the upper and lower bilayer graphene layers, respectively. (**b**) (**i**) The displacement (u_y) field across the shear DW in (**a**). (**ii**–**iv**) Spatial profiles of in-plane piezoelectric, flexoelectric and piezo-flexoelectric polarizations are proportional to the first derivative of displacement ($\partial u_y/\partial x$), second derivative of displacement ($\partial^2 u_y/\partial x^2$) and linear combination of the first and second derivatives of displacement ($A{\cdot}\partial u_y/\partial x + B{\cdot}\partial^2 u_y/\partial x^2$), respectively. (**c**) Two-dimensional in-plane piezo-flexoelectric polarization image. The color denotes the direction of polarization in the inset. Green and blue dots represent AB-CA and AB-AB domains, respectively.

3. Conclusions

In conclusion, tDBG moiré superlattices represent a pristine platform for investigating electromechanical couplings at the mesoscopic scale. Our findings reveal the coexistence of piezoelectricity and flexoelectricity in the DWs of tDBG and offer new ways to manipulate electromechanical couplings in moiré superlattices. The interplay of electronic state transition and polarization competition in a moiré system, such as opposite Chern numbers in twisted transition metal dichalcogenide [26,27], can be derived from polarization competition among ferroelectricity, piezoelectricity and even flexoelectricity [28], which may not only advance our understanding of the electronic phenomena but also show promise for the development of innovative technologies with tailored electronic and mechanical functionalities.

4. Methods

Sample Fabrication. All devices were fabricated using a modified 'tear-and-stack' method (see Figure S1a for details), similar to Ref. [29]. Typical optical images of tDBG devices are shown in Figure S1b.

Scanning Probe Microscopy Measurements. LPFM, cAFM and DART LPFM modes were adopted in this work. Those measurements are carried out on an Oxford Instruments Asylum Research MFP-3D Origin atomic force microscope. ASYELEC-01-R2 probes coated with 5-nm Ti and 20-nm Ir were used in all modes with a spring constant of 2.8 N/m. The typical free resonance frequency is ~75 kHz, and LPFM contact resonance frequency is ~780 kHz.

Supplementary Materials: The following supporting information can be downloaded at https://www.mdpi.com/article/10.3390/sym16111524/s1. Correspondence and requests for materials should be addressed to Y.L. and Y.S.

Author Contributions: Y.L. and Y.S. conceived the experiment. Y.W. and Y.L. performed the AFM measurements. H.Z. and Y.L. fabricated the devices with the help of S.L. T.T. and K.W. provided the bulk BN crystals. Y.L., Y.S., H.Z. and Y.W. analyzed the data. Y.L., Y.S., C.-F.G., H.Z. and Y.W. wrote the paper with input from all authors. All authors have read and agreed to the published version of the manuscript.

Funding: This work was supported by the National Key Research and Development Program of China (2021YFA0715600), National Natural Science Foundation of China (12072150, 12274222 and 12404217), National Science Foundation of Jiangsu Province (BK20220756), Natural Science Foundation of Guangdong Province (2022A1515011773), and National Natural Science Foundation of China for Creative Research Groups (51921003). K.W. and T.T. acknowledge support from the JSPS KAKENHI (21H05233 and 23H02052) and World Premier International Research Center Initiative (WPI), MEXT, Japan.

Data Availability Statement: Data are contained within the article and Supplementary Materials.

Conflicts of Interest: The authors declare no competing interests.

References

1. Catalan, G.; Seidel, J.; Ramesh, R.; Scott, J.F. Domain wall nanoelectronics. *Rev. Mod. Phys.* **2012**, *84*, 119–156. [CrossRef]
2. Nataf, G.F.; Guennou, M.; Gregg, J.M.; Meier, D.; Hlinka, J.; Salje, E.K.H.; Kreisel, J. Domain-wall engineering and topological defects in ferroelectric and ferroelastic materials. *Nat. Rev. Phys.* **2020**, *2*, 634–648. [CrossRef]
3. Meier, D.; Selbach, S.M. Ferroelectric domain walls for nanotechnology. *Nat. Rev. Mater.* **2022**, *7*, 157–173. [CrossRef]
4. Xia, Y.; Ji, Y.; Liu, Y.; Wu, L.; Yang, Y. Controllable Piezo-flexoelectric Effect in Ferroelectric Ba0.7Sr0.3TiO3 Materials for Harvesting Vibration Energy. *ACS Appl. Mater. Interfaces* **2022**, *14*, 36763–36770. [CrossRef]
5. Zubko, P.; Catalan, G.; Tagantsev, A.K. Flexoelectric effect in solids. *Annu. Rev. Mater. Res.* **2013**, *43*, 387–421. [CrossRef]
6. Wang, B.; Gu, Y.; Zhang, S.; Chen, L.-Q. Flexoelectricity in solids: Progress, challenges, and perspectives. *Prog. Mater. Sci.* **2019**, *106*, 100570. [CrossRef]
7. Cao, Y.; Fatemi, V.; Fang, S.; Watanabe, K.; Taniguchi, T.; Kaxiras, E.; Jarillo-Herrero, P. Unconventional superconductivity in magic-angle graphene superlattices. *Nature* **2018**, *556*, 43–50. [CrossRef]
8. Cao, Y.; Fatemi, V.; Demir, A.; Fang, S.; Tomarken, S.L.; Luo, J.Y.; Sanchez-Yamagishi, J.D.; Watanabe, K.; Taniguchi, T.; Kaxiras, E.; et al. Correlated insulator behaviour at half-filling in magic-angle graphene superlattices. *Nature* **2018**, *556*, 80–84. [CrossRef]
9. Sharpe, A.L.; Fox, E.J.; Barnard, A.W.; Finney, J.; Watanabe, K.; Taniguchi, T.; Kastner, M.A.; Goldhaber-Gordon, D. Emergent ferromagnetism near three-quarters filling in twisted bilayer graphene. *Science* **2019**, *365*, 605–608. [CrossRef]
10. Serlin, M.; Tschirhart, C.L.; Polshyn, H.; Zhang, Y.; Zhu, J.; Watanabe, K.; Taniguchi, T.; Balents, L.; Young, A.F. Intrinsic quantized anomalous Hall effect in a moiré heterostructure. *Science* **2020**, *367*, 900–903. [CrossRef]
11. Zheng, Z.; Ma, Q.; Bi, Z.; de la Barrera, S.; Liu, M.H.; Mao, N.; Zhang, Y.; Kiper, N.; Watanabe, K.; Taniguchi, T.; et al. Unconventional ferroelectricity in moire heterostructures. *Nature* **2020**, *588*, 71–76. [CrossRef] [PubMed]
12. Klein, D.R.; Xia, L.-Q.; MacNeill, D.; Watanabe, K.; Taniguchi, T.; Jarillo-Herrero, P. Electrical switching of a bistable moiré superconductor. *Nat. Nanotechnol.* **2023**, *18*, 331–335. [CrossRef] [PubMed]
13. Kazmierczak, N.P.; Van Winkle, M.; Ophus, C.; Bustillo, K.C.; Carr, S.; Brown, H.G.; Ciston, J.; Taniguchi, T.; Watanabe, K.; Bediako, D.K. Strain fields in twisted bilayer graphene. *Nat. Mater.* **2021**, *20*, 956–963. [CrossRef] [PubMed]
14. McGilly, L.J.; Kerelsky, A.; Finney, N.R.; Shapovalov, K.; Shih, E.M.; Ghiotto, A.; Zeng, Y.; Moore, S.L.; Wu, W.; Bai, Y.; et al. Visualization of moire superlattices. *Nat. Nanotechnol.* **2020**, *15*, 580–584. [CrossRef]
15. Li, Y.; Wang, X.; Tang, D.; Wang, X.; Watanabe, K.; Taniguchi, T.; Gamelin, D.R.; Cobden, D.H.; Yankowitz, M.; Xu, X.; et al. Unraveling Strain Gradient Induced Electromechanical Coupling in Twisted Double Bilayer Graphene Moiré Superlattices. *Adv. Mater.* **2021**, *33*, 2105879. [CrossRef]
16. Zhang, H.; Wei, Y.; Li, Y.; Lin, S.; Wang, J.; Taniguchi, T.; Watanabe, K.; Li, J.; Shi, Y.; Wang, X.; et al. Layer-Dependent Electromechanical Response in Twisted Graphene Moiré Superlattices. *ACS Nano* **2024**, *18*, 17570–17577.
17. Kerelsky, A.; Rubio-Verdú, C.; Xian, L.; Kennes, D.M.; Halbertal, D.; Finney, N.; Song, L.; Turkel, S.; Wang, L.; Watanabe, K.; et al. Moiréless correlations in ABCA graphene. *Proc. Natl. Acad. Sci. USA* **2021**, *118*, e2017366118.
18. Alden, J.S.; Tsen, A.W.; Huang, P.Y.; Hovden, R.; Brown, L.; Park, J.; Muller, D.A.; McEuen, P.L. Strain solitons and topological defects in bilayer graphene. *Proc. Natl. Acad. Sci. USA* **2013**, *110*, 11256. [CrossRef]
19. Jungk, T.; Hoffmann, Á.; Soergel, E. Quantitative analysis of ferroelectric domain imaging with piezoresponse force microscopy. *Appl. Phys. Lett.* **2006**, *89*, 163507. [CrossRef]
20. Zhang, S.; Song, A.; Chen, L.; Jiang, C.; Chen, C.; Gao, L.; Hou, Y.; Liu, L.; Ma, T.; Wang, H.; et al. Abnormal conductivity in low-angle twisted bilayer graphene. *Sci. Adv.* **2020**, *6*, eabc5555. [CrossRef]
21. Rosenberger, M.R.; Chuang, H.-J.; Phillips, M.; Oleshko, V.P.; McCreary, K.M.; Sivaram, S.V.; Hellberg, C.S.; Jonker, B.T. Twist Angle-Dependent Atomic Reconstruction and Moiré Patterns in Transition Metal Dichalcogenide Heterostructures. *ACS Nano* **2020**, *14*, 4550–4558. [CrossRef]

22. Li, Y.; Xue, M.; Fan, H.; Gao, C.-F.; Shi, Y.; Liu, Y.; Watanabe, K.; Tanguchi, T.; Zhao, Y.; Wu, F.; et al. Symmetry Breaking and Anomalous Conductivity in a Double-Moiré Superlattice. *Nano Lett.* **2022**, *22*, 6215–6222. [CrossRef]
23. Zhang, S.; Xu, Q.; Hou, Y.; Song, A.; Ma, Y.; Gao, L.; Zhu, M.; Ma, T.; Liu, L.; Feng, X.-Q.; et al. Domino-like stacking order switching in twisted monolayer–multilayer graphene. *Nat. Mater.* **2022**, *21*, 621–626. [CrossRef] [PubMed]
24. Gruverman, A.; Kalinin, S.V. Piezoresponse force microscopy and recent advances in nanoscale studies of ferroelectrics. *J. Mater. Sci.* **2006**, *41*, 107–116. [CrossRef]
25. Lebedeva, I.V.; Lebedev, A.V.; Popov, A.M.; Knizhnik, A.A. Dislocations in stacking and commensurate-incommensurate phase transition in bilayer graphene and hexagonal boron nitride. *Phys. Rev. B* **2016**, *93*, 235414. [CrossRef]
26. Park, H.; Cai, J.; Anderson, E.; Zhang, Y.; Zhu, J.; Liu, X.; Wang, C.; Holtzmann, W.; Hu, C.; Liu, Z.; et al. Observation of fractionally quantized anomalous Hall effect. *Nature* **2023**, *622*, 74–79. [CrossRef] [PubMed]
27. Foutty, B.A.; Kometter, C.R.; Devakul, T.; Reddy, A.P.; Watanabe, K.; Taniguchi, T.; Fu, L.; Feldman, B.E. Mapping twist-tuned multiband topology in bilayer WSe2. *Science* **2024**, *384*, 343–347. [CrossRef]
28. Zhang, X.-W.; Wang, C.; Liu, X.; Fan, Y.; Cao, T.; Xiao, D. Polarization-driven band topology evolution in twisted MoTe2 and WSe2. *Nat. Commun.* **2024**, *15*, 4223. [CrossRef]
29. Wong, D.; Nuckolls, K.P.; Oh, M.; Lian, B.; Xie, Y.; Jeon, S.; Watanabe, K.; Taniguchi, T.; Bernevig, B.A.; Yazdani, A. Cascade of electronic transitions in magic-angle twisted bilayer graphene. *Nature* **2020**, *582*, 198–202. [CrossRef]